Effect of pH on Mg(OH)2 film evolution on corroding Mg by in situ kinetic Raman mapping (KRM)

Alina Maltseva, Viacheslav Shkirskiy, Grégory Lefèvre, Polina Volovitch

Corrosion Science 153 (2019) 272–282

Contents lists available at ScienceDirect

Corrosion Science

journal homepage: www.elsevier.com/locate/corsci

Effect of pH on $Mg(OH)_2$ film evolution on corroding Mg by in situ kinetic Raman mapping (KRM)

Alina Maltseva, Viacheslav Shkirskiy[1], Grégory Lefèvre, Polina Volovitch*

Chimie ParisTech, PSL University, CNRS, Institut de Recherche de Chimie Paris (IRCP), F-75005, Paris, France

ARTICLE INFO

Keywords:
A. Magnesium
A. Brucite
B. In-situ Raman spectroscopy
C. Aqueous corrosion
C. Surface film evolution

ABSTRACT

$Mg(OH)_2$ films evolution at initial stages of Mg aqueous corrosion was studied by in-situ Raman spectroscopy adapted for kinetic Raman mapping (KRM). Crystalline $Mg(OH)_2$ (brucite) formed in situ from the first minutes of reaction. KRM evidenced a threshold-like $Mg(OH)_2$ growth kinetics for areas where black filaments were later formed, linear kinetics for visually intact areas at pH 9–10 and parabolic law for intact areas at pH > 11. The $Mg(OH)_2$ morphology expected from in-situ Raman scattering of surface OH groups correlated well with ex-situ microscopic observations. A dissolution-precipitation model of $Mg(OH)_2$ layer evolution was applied to explain the experimental observations.

1. Introduction

1.1. Necessity of in-situ characterization of surface films evolution on corroding Mg

Magnesium based alloys are attractive to multiple applications including automotive, aerospace, biomedical industries [1], however in contact with water or in humid atmosphere they are subject to corrosion [2,3]. Aqueous corrosion of active materials like magnesium and its alloys is strongly affected by chemistry and morphology of the oxide / hydroxide layer at the interface metal /solution. Multiple ex-situ characterizations were published for corroded magnesium alloys, demonstrating a double layer film: an inner thin oxide MgO and an external $Mg(OH)_2$ and have a complex porosity [2,4–10]. As for the attribution of the structure, the ex-situ characterizations has confirmed the presence of crystalline MgO [4] and crystalline $Mg(OH)_2$ (existing in the only crystalline structure referred as brucite [11] by low angle X ray diffraction (GIXRD) and by transmission electron microscopy with selected area electron diffraction (SAED) [6,12]). The presence of amorphous hydroxide at the interface oxide-hydroxide is also defended [2,4–9,13,14].

The oxide/hydroxide layer is often considered as a reason of a barrier protection of Mg at the early stages of aqueous corrosion [15,16] in particular in strong alkaline solutions when a stable protective surface film can be formed [17–20]. Localized film damage appears in neutral solutions containing chloride, sulphate, or nitrate anions [16,21] and the corroded area looks black. This black color of the corroded area was previously attributed to the cracking and the detachment of small Mg particles [22,23], however the mixture of $MgO/Mg(OH)_2$ in the dark corroded areas was reported as well [6,24]. Magnesium hydroxycarbonates [25–27], $MgCl_2{\cdot}6H_2O$, $Mg_3(OH)_5Cl{\cdot}4H_2O$ and $5(Mg(OH)_2){\cdot}MgCl_2$ were also identified after corrosion in NaCl containing aqueous solutions [21]. The presence of Cl in the inner oxide layer has been shown [5,28], that was assumed as the evidence of the aggressive species key role in the film breakdown mechanism.

Besides aggressive species penetration, the film breakdown can be provoked by mechanical stresses due to low Pilling-Bedworth ratio for Mg/MgO. This also leads to the film porosity and cracking. The volume changes resulting from hydration/dehydration of $MgO/MgO{\cdot}H_2O/Mg(OH)_2$ films [5,13,29–31] also contributes to the film cracking [31]. The stability of an external surface film limiting water and aggressive species access to the internal MgO layer can be regarded as an important factor in corrosion mechanism [20]. From the previous ex-situ studies, this film is formed by $Mg(OH)_2$ (brucite) crystals. The application of the mechanisms using stability of brucite film as the explanation of the pH effect on Mg reactivity needs hence a clear confirmation that the brucite is present on corroding surface during reactivity and is not formed ex-situ on dry surface during sample preparation and / or surface analysis. If confirmed, the mechanisms of its formation and factors of its stability need to be understood. Thus, one of the objectives of the present work is to confirm in situ the existence of the surface $Mg(OH)_2$ film and its

* Corresponding author.
E-mail address: polina.volovitch@chimie-paristech.fr (P. Volovitch).
[1] Present address: Department of Chemistry, University of Warwick, Coventry, CV4 7AL, UK.

https://doi.org/10.1016/j.corsci.2019.03.024
Received 18 January 2019; Accepted 19 March 2019
Available online 26 March 2019

crystallinity during aqueous corrosion of Mg and to explore the mechanisms of its formation in aqueous solutions.

Starting from the work of Vermilya [32], brucite film formation on corroding Mg is assumed by dissolution-precipitation mechanism. In multiple works the loss of barrier properties of the corrosion products films on Mg or their harmful autocatalytic effect on the hydrogen evolution reaction are attributed to dissolution-precipitation control of the film formation and breakdown [33–35]. The dissolution-precipitation hypothesis, even if looks very reasonable, stays speculative until the film evolution by dissolution-precipitation mechanism is proven by in-situ analysis. Moreover, one can expect that the experimental kinetics of corrosion products formation cannot be described only by precipitation from the solution bulk, the film formation rate being directly related to the corrosion rate and the local conditions at the metal surface [36].

The in-situ kinetics measurement of the surface films evolution on corroding materials and the effect of solution composition on the film growth and breakdown could be very helpful to support proposed in the literature reactivity mechanisms [2,3,18,37,38]. Moreover, the hypotheses about the aqueous reactivity mechanisms, advanced using the results of characterization of dry surface films under high vacuum, can lead to incorrect interpretations because of significant chemical and morphological modifications and hence significant difference between the analyzed surface and the surface reacting in aqueous environments. Some recent in-situ TEM studies [13,14] also have clearly demonstrated that the evolution between the crystalline MgO, amorphous $Mg(OH)_2$ and crystalline brucite can appear because of the sample preparation for the surface analysis and directly under the beam, underlying the importance of in-situ characterization of the film during aqueous reactivity.

To approach the mass balance and the mechanisms of Mg corrosion, real time reactivity measurements by local electrochemistry [39–42], by coupling electrochemical technics and chemical solution analysis [43–45], different types of Time Lapse Microscopy [35,46,47] or volumetric measurements [43,46,48] were reported. The effects of the alloy composition [49,50] and solution composition [43,44,51–54] on the reactivity of many Mg alloys were communicated and discussed in terms of possible modification of the surface chemistry. In contrast, the only published in-situ study of the film growth kinetics on Mg corroding in aqueous solution reported a linear increase of the average film thickness with time measured by ellipsometry [16] without no mechanistic insight. We were not able to find any in-situ chemical analysis of the corroding Mg surfaces in aqueous solution, which could prove or disprove the film formation and breakdown mechanisms. The latest indicates a gap in the knowledge related to the absence of a methodology able to analyze in situ the surface evolution of corroding in aqueous solutions Mg.

The study of the surface films on corroding Mg is complicated by the fact that Mg reactivity is usually inhomogeneous and the initiation of the localized processes is unpredictable. Some works reported the initiation of localized corrosion at grain boundaries, near cathodic impurities and some correlations were also reported between the crystallographic orientation of the grains and the thickness of the oxide film [55–58]. However, the film growth initiation and the film breakdown stay stochastic processes and the understanding of the film evolution needs a statistically valid and spatially resolved (μm-scale) observation. Measurement of the film growth and breakdown kinetics in one point is hence not representative. An ideal in-situ surface analysis should be hence able to monitor the film evolution continuously with high enough lateral resolution, sensitive to chemical composition, and fast enough to provide in-situ measurements on representative areas.

The first objective of the current work is hence methodological - to propose a methodology able to analyze the surface evolution of corroding in aqueous solutions Mg in situ, on large surfaces but with good spatial resolution (several μm) and in a quantitative way in order to extract the kinetics data. The material science objective is to confirm in situ the presence of crystalline $Mg(OH)_2$ (brucite) during aqueous corrosion of Mg, to evaluate the kinetics of the $Mg(OH)_2$ film growth and breakdown and approach the film evolution mechanisms.

1.2. Opportunities of in-situ kinetic Raman mapping

The present work proposes an approach combining the potential of in-situ kinetic measurement using Raman spectroscopy and the advantages of mapping mode achieved with Confocal Raman Mapping (CRM) in order to study the surface evolution in aqueous environment in mapping mode, namely extracting kinetics of local chemical and morphological evolution, of film growth and film breakdown. It is named below “in-situ kinetic Raman mapping” or KRM.

Continuous mapping of chemical specification with good (μm) lateral resolution and fast enough to provide in-situ measurements on large surfaces is possible with Confocal Raman Mapping (CRM) [59,60]. The CRM has however never been applied in kinetics studies even if in-situ Raman spectroscopy in application to corroded surfaces is developed since 1980th [61–70]. It is widely used to identify corrosion products formed locally during corrosion or products formed in electrochemical reactions and to survey the system evolution in a semi-quantitative way [59,71]. However, most of these works were focused on the identification of corrosion products in selected locations and the quantitative film evolution was even not considered. At the same time, despite the complexity of the quantitative data treatment in Raman spectroscopy [72], it has been possible to extract the kinetics of the chemical evolution from Raman spectra [73] in case of phase transformations of polymers [74] or inorganic compounds [75–77], as well as to use Raman spectroscopy in biology [78,79]. The intensity of Raman scattered light from a sample is proportional to the number of Raman active bonds in the analyzed volume [72] which can be used for a semi-quantitative analysis and monitoring of the growth kinetics using the spectra normalization. Although the Raman spectra of crystals can be influenced by their size and shape (absolute scattering intensity, relative intensities and band shapes can be affected [80]), these effects usually take place only for nano-size dimensions, 5–50 nm [81] and also could be turned in an advantage in order to access morphology and crystal size.

To sum up, the three main objectives of the present work are

1) to propose an experimental approach and a way of data treatment in Confocal Raman Mapping which is able to provide quantitative information and measure in-situ the kinetics of growth or transformation of surface film in mapping mode (KRM) and demonstrate the validity of obtained KRM;
2) to apply KRM on large surfaces of commercially pure Mg in Cl-containing aqueous solutions of different pH (from unbuffered to 0.1 M NaOH) in order to prove the presence of $Mg(OH)_2$ film in situ, to verify its crystallinity and to obtain the local kinetics of brucite growth in the areas which show different surface appearance after the experiment;
3) to correlate the obtained kinetics tendencies with $Mg(OH)_2$ film formation and breakdown mechanisms for spontaneously corroding in aqueous solution Mg and precise the effect of pH on these mechanisms

2. Materials and methods

2.1. Materials

Commercially available magnesium (99.9%, see Table 1 for impurities content) in the form of 0.5 mm thickness foils for Mg 1 and coupons of 2 cm thickness for Mg 2.3 cm^2 Mg coupons were grounded with 800, 1200, 2400, 4000 SiC grinding paper, using ethanol as a lubricant, rinsed with ethanol and dried by compressed air. All electrolytes were prepared using analytical grade reagents (Sigma Aldrich)

Table 1
Impurities level in studied materials.

	Element (ppm)							
	Mg	Fe	Mn	Al	Cu	Ni	Si	Zn
Mg 1	Bal.	280	170	70	20	< 10	50	< 20
Mg 2	Bal.	36	38	42	10	5	86	–

and distilled water. The initial pH of NaCl solutions was adjusted to the targeted values from 8.5 to 10.5 by 0.1 M NaOH solution and to the theoretical pH 13 by the addition of solid NaOH to obtain 0.1 M solution.

2.2. In-situ Raman spectroscopy for kinetic Raman mapping (KRM)

2.2.1. Acquisition conditions and justification of quantitative measurement

For in-situ mapping, a Confocal Raman Microscope (Renishaw InVia) with a long distance objective (Leica, magnification ×50 and numerical aperture NA = 0.5, working distance 8 mm) was used with a green laser (532 nm, 50 mW). A freshly prepared Mg sample was directly mounted in a 3D printed polylactic flow cell with a glass optical window (Fig. 1). The thickness of the liquid layer on the sample was about 1 mm. Solution was systematically renewed using a syringe pump before each map in order to remove the bubbles which affect the laser focusing. In the selected experimental conditions, the analyzed depth was estimated as 59 µm (see Appendix A for the procedure), and the laser spot diameter as 1.3 µm. For a typical experiment a selected area of 1 × 1 mm was scanned with a step of 50 µm in the high resolution (HR) streamline acquisition CRM mode with the exposure time of 0.2 s for each location. The total time of each map recording was about 2 min. The mapping was repeated every 5–10 min. The signal of water, contained in the major part of the analyzed volume, was used to normalize the in-situ spectra and to monitor the local growth kinetics. Such a treatment is justified by the fact that the average hydroxide layer thickness on corroded Mg reported in the literature (from about 100 nm to 2–3 microns [82]) is significantly smaller than the analyzed by Raman depth.

2.2.2. Spectral region selection for mapping and data treatment procedure

The Raman spectra were pre-processed using Wire 4.2. software. The preprocessing included cosmic ray removal, noise removal, baseline subtraction and signal normalization: spectra were normalized in a way that the baseline corresponded to 0, and the maximum of the intensity of liquid water (3415 cm^{-1}) corresponded to 1. The area (A) of the peak with the Raman shift 3652 cm^{-1} corresponding to A_{1g} O-H stretch vibrations in $Mg(OH)_2$ [83] was used to monitor the spatial distribution of brucite and its growth kinetics for several reasons.

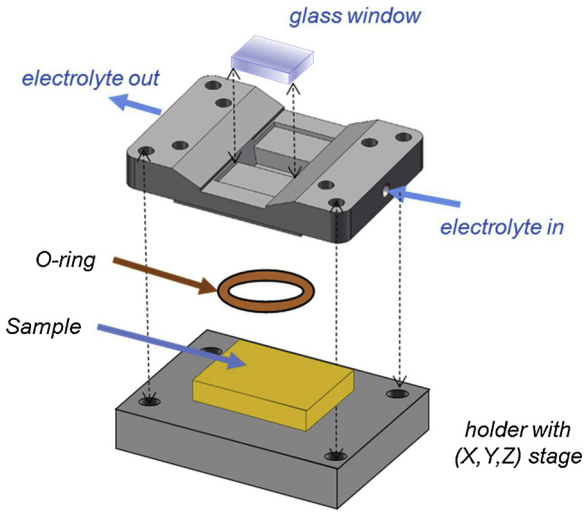

Fig. 1. Schematics of 3D printed thin layer cell for in-situ Raman mapping experiments.

Firstly, according to the literature, this peak is the most intensive and the narrowest (as can be also seen in our results, see Appendix B showing all the peaks on the dry surface). Moreover, according to [84], the low-frequency Raman peaks offer no substantial information on thin layers due to the low optical absorption coefficient of wide band gap $Mg(OH)_2$; by consequence, the material analysis and quantification of thin layers cannot be performed using these peaks. In contrast, the peak appearing at very high frequencies was observed in this work clearly from bulk to monolayers owing to its large Raman scattering cross-section under visible excitation.

Secondly, the position in the OH region (after 3000 cm^{-1}) is the most convenient for the rapid simultaneous acquisition and mapping of both, $Mg(OH)_2$ and water signals evolution, which is necessary for quantitative analysis. The peaks at 280, 444 and 775 cm^{-1} being too far from the characteristic water peaks, they are less interesting from analytical point of view because of the grating limitations. Since the normalizing procedure requiring both, analyzed peak and water peak, the time resolution (larger spectral region to acquire) or the analysis sensitivity (shorter acquisition time per point) will be degraded.

In the purpose to verify the crystallinity, the in-situ and ex-situ spectra where compared. If the crystallinity of $Mg(OH)_2$ formed in situ and ex situ is different, the position and the shape of the peak should change, the peaks of amorphous or nanocrystalline compound being significantly different [85]. Additionally, to confirm the 3D crystallinity, the presence of the low frequency peaks was also verified in situ and ex situ. This was necessary because the sensitivity of the A_{1g} OH stretch vibrations is very high; they were detected in very thin 2D structures of several monolayers, while the presence of the fingerprint (3 peaks) can be considered as a proof of a crystalline 3D bulk [84].

The maps of the selected $Mg(OH)_2$ peak areas acquired at different times of the experiment were exported in the asci format and were treated with a homemade software. The software was able to verify for each location of the map if the peak evolution as a function of time can be described by a selected kinetics law (linear, parabolic, threshold like, etc…) and to present in the same color the points in which the film growth is described by the same kinetics law. Another mapping mode was used to ascribe a color code to the time at which the film growth kinetics changes, mapping in such a way the film breakdown time.

2.3. Ex-situ analysis

In selected locations, additional ex-situ Raman spectra were obtained after the experiment using a short distance Leica objective with NA 0.75 and longer exposure times, typically 10 s. The morphology of corroded surfaces was also observed using scanning electron microscope (SEM-FEG Gemini 1530®) at applied voltage of 1–10 kV.

3. Results

3.1. Visual surface evolution and characteristic morphologies of corroding Mg

Fig. 2 shows a typical evolution of Mg surface with development of a black filament visible in an optical microscope during Mg immersion in the thin layer cell with 0.1 M NaCl solution at initial pH 9–10. The filament appeared typically on less pure Mg 1. Another corrosion morphology, observed on both types of Mg, was the formation of a black points (will be shown later), which did not evolve with time visually during the time of the experiment. These points will be shown later. Even if only one example is shown, the evolution features were similar for all the experiments when the initial solution pH starting from neutral to pH 10.5. One should also note that after approximately

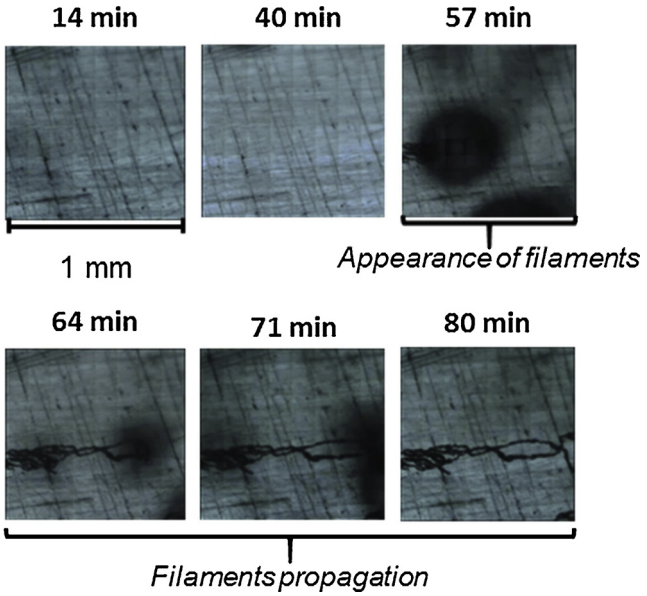

Fig. 2. Typical example of surface evolution of Mg 1 corroding in 0.1 M NaCl solution at initial pH 9. Black areas associated with the filaments and unchanged intact zones are visible.

40 min of the experiment the downstream solution pH approaches 10 for all the experiments in which the initial solution pH was between 8 to 10. This value of pH is coherent with the pH of brucite precipitation and its buffering effect [86]. As expected from the literature [87], the black filaments of 10–20 μm width appeared randomly after approximately 20 min of the experiment. The propagation of the "head" of the filament was accompanied by a significant gas evolution. In Fig. 2, the gas is visible as circular shadows. The surface appearance outside the filaments did not change neither in visual observation after the experiment nor in optical images taken in situ by the microscope. In further discussion, the term "intact region" will be used for such areas. For the experiments made in strongly alkaline solutions (pH > 12), during the time of the experiments black filaments did not appear even for Mg 1. The surface evolution at pH 13 is not shown because no visible in optical microscope surface modification was detected in these conditions during the time of the experiment.

3.2. In-situ Raman spectra typical for characteristic surface morphologies

In-situ Raman spectra in the range of 3000–4000 cm^{-1} recorded in different locations of the surface revealed small but systematic differences in the OH region as illustrated by examples in Fig. 3. All the spectra in the figure are normalized by the water signal as described in the experimental section. The presence of microcrystalline brucite is evidenced by a strong peak at 3652 cm^{-1} corresponding to A_{1g} O—H stretching mode in $Mg(OH)_2$ crystals [83].

There was no peak position difference between the last in-situ and the recorded after solution removal ex situ Raman spectra indicating that the crystalline species observed ex situ where already present in situ. The 3 D crystallinity was also confirmed in broad scans (not shown) by the presence of peaks at 443 cm^{-1} and 280 cm^{-1} corresponding to lattice vibrations, A_{1g} and E_g respectively. More Raman spectra characteristic for different locations can be consulted in Appendix B (Fig. S1). On low purity Mg (Mg 1) the black points did not develop into the filaments. Spectra of these spots did not show the appearance of the second peak.

The figure evidences the appearance of two types of "satellites" in Raman spectra: at 3675 cm^{-1} and 3710 cm^{-1}, appearing at high pH and in black filaments at moderate pH. No satellites were detected in situ in intact areas at neutral pH. We did not found any publication reporting clearly these high frequency satellites in the experimental Raman spectra of crystalline brucite. They were also not listed for nanocrystalline brucite [88]. We noted also that the appearance of these peaks was not affected by Cl^- content and that no carbonate contamination was detected (no peaks between 1000 and 1100 cm^{-1}). This argument let us tentatively interpret these peaks to specific surface vibrations of Mg − OH surface groups with different surface crystalline plane. According to the DFT calculations, the surface OH groups should give satellite peaks with frequency increasing in order of the increase of the surface energy (frequency of (0001) lower than frequency of (1010) [85,89]. An alternative explanation can be a microstructure distortion or phase transition making Raman active usually forbidden the IR active mode as previously observed at high pressures [90] or that the crystal is hydrated, however we din't found any reference Raman spectra for hydrated magnesium hydroxide. In such an interpretation, the presence of satellites can be tentatively used for the survey of the morphological evolution of the crystals [80]. For hexagonal close packed (hcp) crystals, including brucite, the platelet shape is typical and the growth plane (the largest surface) corresponds to the crystalline plane with the lowest energy (0001) [11,91]. The satellite peaks at high pH indicating the higher fraction of high energy surfaces, they reflect hence less advanced grain growth and by consequence smaller expected crystal size.

Comparison of the optical images of the surface and the in situ recorded maps representing the spatial distribution of the normalized peak area of the principal peak at 3652 cm^{-1} at different pH (examples in Fig. 4) illustrates, that at pH 13 the brucite film looks homogenous while at pH 9–10 the signal is significantly higher in black filaments. A statistical analysis of the ratio of the peak areas A(3675 cm^{-1} or 3710 cm^{-1})/A(3652 cm^{-1}) at different times of the experiment has shown that after an initial period at which the satellite peaks cannot be separated from the noise, the ratio stays constant at pH 13 (around 0.17 +/− 0.07 for high purity Mg 2 and around 0.07 +/− 0.07 for low purity Mg 1).

3.3. Ex-situ morphologies of $Mg(OH)_2$ film

Ex-situ Scanning Electron Microscopy (SEM) (Fig. 5) demonstrated that brucite particles present regular close to hexagonal platelet-like morphology with the thickness of the platelets in order of 5–7 nm for all observed areas, while the platelet diameter varied significantly in function of local solution composition. Bigger particles were formed in intact areas and in black spots with the platelets diameter between 200 and 1000 nm. The platelet diameter was less than 50 nm inside the filaments and below 100 nm at pH 13. The presence of satellites in in-situ Raman spectra correlated hence well with the lowering of the brucite crystal size. The EDS analysis of black spots (not black filaments) made at 20 kV revealed the presence of nano-sized particles containing Ca or the underlying Si-rich particles of μm size (Appendix C). A simple interpretation of the black spots with no development of filaments but high quantity of precipitated brucite can be hence in terms of impurities (coming probably from polishing procedure) acting as nucleating centers and accelerating local precipitation and grain growth around these nuclea.

3.4. $Mg(OH)_2$ growth and breakdown kinetics

Shaded areas in Fig. 3a illustrates how the evolution of the peak area (noted as A here and later) was evaluated for kinetic measurements. The procedure described in Experimental section was applied to plot the kinetics of brucite growth on Mg 1 and Mg 2 surfaces (typical size 1 × 1 mm) at different pH. The kinetic plots were made with different spatial resolutions to verify that the kinetic law does not depend on the resolution. At the areas in which gas bubbles were formed they caused the defocusing of the laser beam that disturbed the local measurements. Despite systematic solution renewal it was impossible to

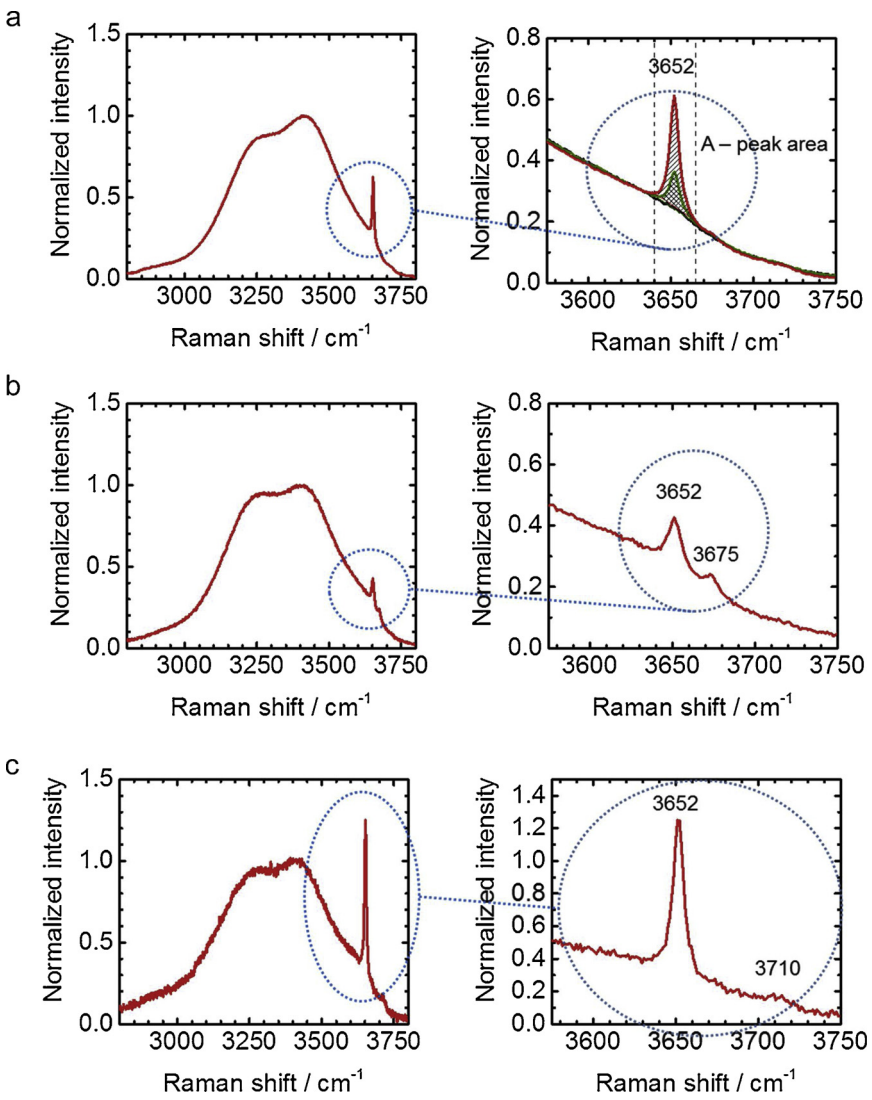

Fig. 3. Typical normalized in-situ Raman spectra of corroding Mg in 0.1 M NaCl solution with different initial pH. (a) intact area at pH 9; (b) intact area at pH 13, (c) black filament at pH 9. The way how the peak area (A) was evaluated for kinetic measurement is also illustrated in figure (a).

eliminate completely the bubbles from the head of the filament. The times at which at selected locations the gas bubble disturbed the measurement were excluded from the kinetics analysis of these points.

Statistical analysis of the maps obtained on both Mg types and at different pH and Cl^-- concentrations revealed for intact areas two typical kinetics of the brucite growth illustrated in Fig. 6a. At pH 13 the brucite evolution is characterized by the kinetics which could be described by a parabolic law (the slope of the graph logA-log(time) was close to 0.5). At pH 9, $Mg(OH)_2$ growth in the intact region is linear with time (the slope 1 of the logA-log(time) plot). Interestingly, the increase of Cl concentration (Fig. 6b) seems to increase the quantity of the formed brucite in intact areas in the first 20 min of experiment, but doesn't seem to modify the kinetics law at this stage (slope of log-A log (time) curve stays close to 1 for different concentrations of Cl^- after approximately ten minutes of the reaction). Very different film growth kinetics (Fig. 6c, circles (red in web version of the article)) was observed in the areas identified at the end of the experiment as black filaments and black points. The curve presented in Fig. 6c initially follows the same kinetic law as an intact region and then shows a threshold-like increase.

Statistical data treatment using KRM confirmed that this type of kinetics is associated with the proximity of black filaments and black spots and that the time of the jump in the kinetics curve (Fig. 7a) coincides with the first visual observation of filament in studied zone. In Fig. 7a the color code reflects the time of the jump in the $Mg(OH)_2$ growth kinetics curve for the experiment presented in Fig. 2. It is clearly seen on the map that the time development of the filament in optical images (Fig. 2) correlates with the change in the brucite growth kinetics (Fig. 7a). Using the map shown in Fig. 7a, it is also possible to plot the fraction of the surface with "broken" film as a function of time (Fig. 7b). At times more than 10–15 min the breakdown kinetics could be approximated by a linear law which is coherent with the previously reported filament growth under anodic polarization [40]. The initial time period is difficult to interpret because the points considered by the software as "breakdown" points corresponds to the initial inhomogeneity of the surface.

4. Discussion

4.1. Role of dissolution – precipitation processes for $Mg(OH)_2$ film growth

Numerous works justify the properties of corroding Mg by dissolution-precipitation processes in the surface films. The origin of the $\log_{10}$ relationship of pitting potential with Cl^- concentration was discussed in terms of the solubility product of magnesium hydroxide [92]. Recently, enhanced hydrogen evolution at the $Mg(OH)_2$ covered Mg

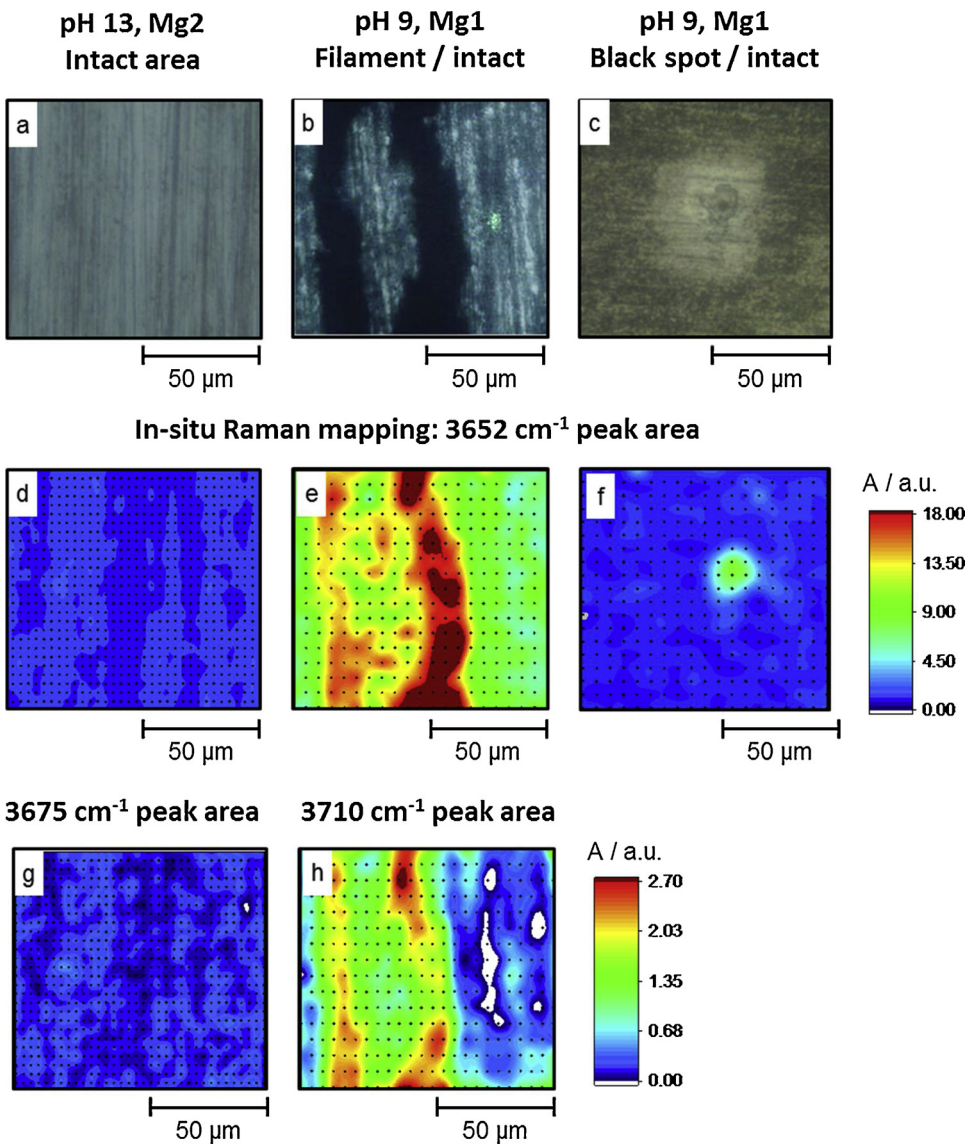

Fig. 4. Examples of different surface appearances ((a)-(c)) observed at different pH, as indicated, and corresponding high resolution in-situ maps of peak area, A. For (d)-(f) - area of 3652 cm^{-1} peak; for (g)- area of 3675 cm^{-1} peak and for (h) – area of 3710 cm^{-1} peak are plotted.

surface compared with pristine Mg [34] was attributed to the enhancement of the self-dissociation of water on corrosion products in order to precipitate released Mg^{2+} ions from a supersaturated condition. Other authors speculated the disruption of the oxide/hydroxide film when an anodic current is available and environmental conditions can induce de-passivation [35] to explain the generation of streams of bubbles at the corrosion front. Such speculations look reasonable but could be stronger if the film evolution by dissolution-precipitation mechanism is proven in situ.

The platelet morphology typical for the precipitated $Mg(OH)_2$ [5,11,93] which was observed previously in slightly alkaline solutions and in all the conditions of our work, including strongly alkaline pH and inside the filaments, is coherent with the mechanisms including precipitation and grain growth with dissolution of high energy surfaces and development of the low energy basal surface. These ex situ observations however could not be considered alone because they cannot confirm that observed crystals are formed during the experiment and not during solution drying or sample preparation and even during observation under high vacuum and in high energy beam.

The presented in situ results could reinforce the ex situ observations. First of all, considering the effect of pH and surface location on the evolution of not only the peak at 3652 cm^{-1} but also the distribution and the evolution of the peaks at 3675 cm^{-1} and 3710 cm^{-1}, the evolution of the crystal size and morphology can be evaluated in situ. Secondly, the kinetics of the film growth could be considered to verify the mechanism of its formation.

The in situ spectra obtained for Mg reacting in solutions with pH 13 show stable and uniformly distributed intensity of different peaks with a constant ratio of peak surfaces A(satellite)/A(3652 cm^{-1}) at different times of the experiment. This can be interpreted as the formation of a uniformly distributed hydrated layer with a relatively constant grain morphology with high fraction of high energy surfaces on the particles, which can be ascribed by high nucleation and slow crystal growth rates. It is also coherent with the results of Henrist et al. [11] who noted very small particle size when $Mg(OH)_2$ is solution precipitated from $MgCl_2$ and NaOH.

One should note that particles in principle could be agglomerates of many small crystals, however the high resolution SEM demonstrated very similar and specific platelet shape of particles and did not evidence agglomeration, indicating that in our experiment the particles are the most probably isolated crystals. Parabolic film growth kinetics indicates diffusion limitation of the film growth. Such kinetics of the film growth

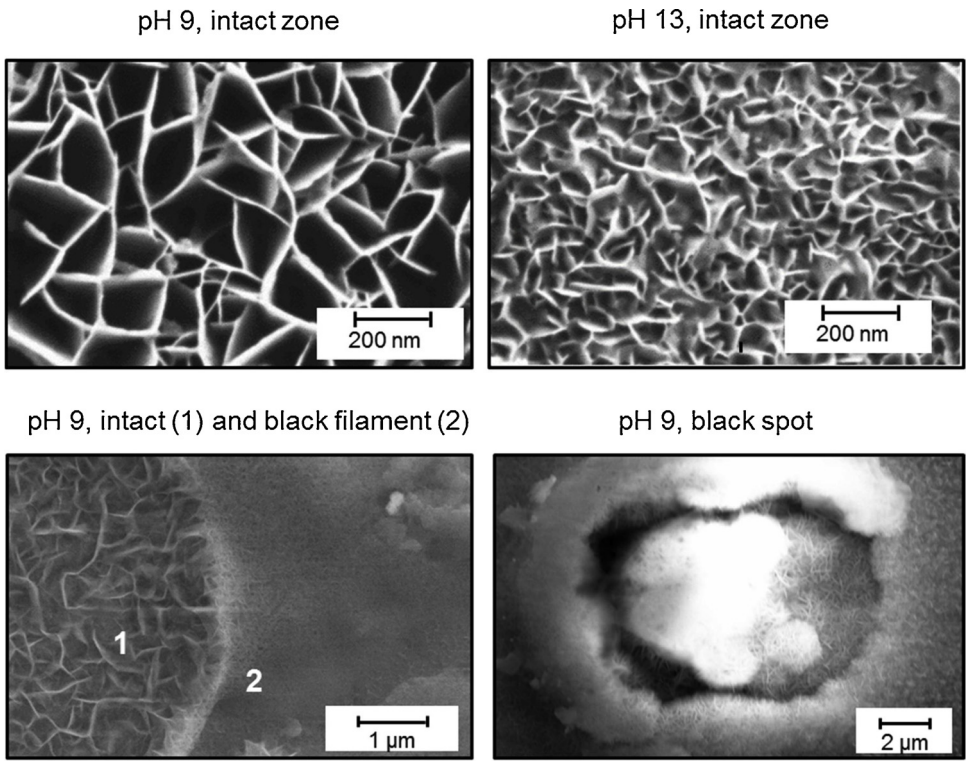

Fig. 5. Typical ex-situ secondary electron images of the Mg surface after 2 h of immersion in 0.1 M NaCl solution. Accelerating voltage 1 kV for intact zones and 10 kV for other images.

is typical for passive films [94,95] and is schematically presented by arrows numbered "1" in Fig. 8 (left, green arrows in the web version of the paper). In the figure diffusion step is attributed to Mg^{2+} diffusion from the metal to the solution; however, oxygen vacancies diffusion can be also considered here. Unfortunately, our data cannot be used to distinguish between the different diffusing species.

For the Mg surfaces immersed in slightly alkaline conditions in situ spectra evolution before the film breakdown indicates insignificant contribution of the satellite peaks to the Raman signal, suggesting more developed surface corresponding to the basal plane and hence

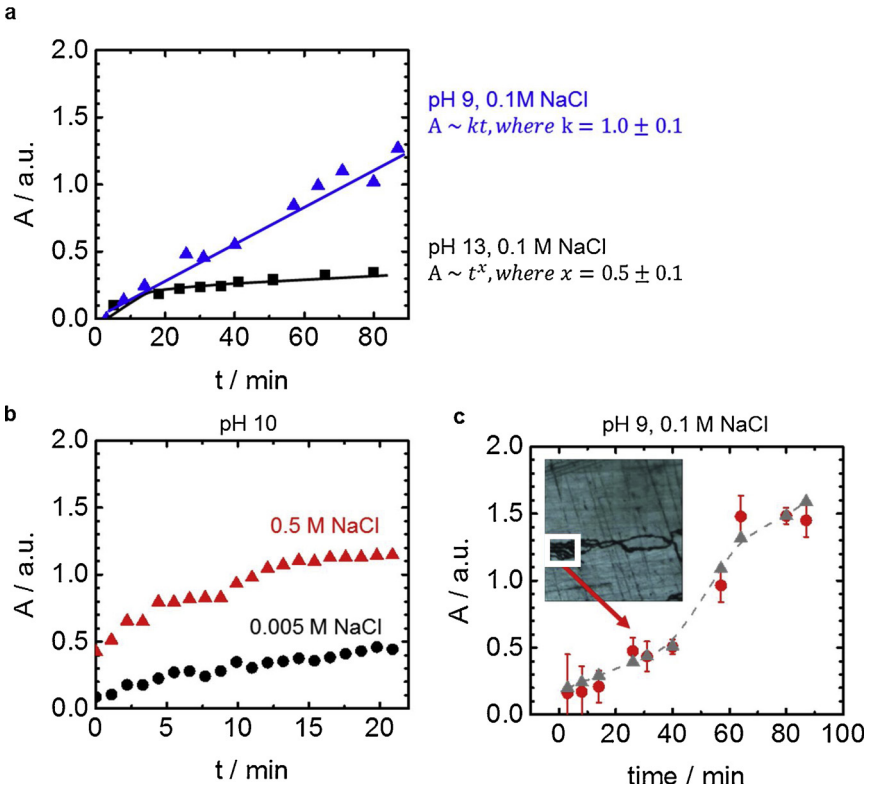

Fig. 6. Evolution of normalized peak area A (3652 cm^{-1}, see Fig. 3a how A is measured) with time for different solution pH and Cl- concentration in the electrolyte (as indicated) reflecting local kinetics of the brucite growth on: (a, b) "intact" regions, (c) black filaments. A threshold sharp increase in fig. (c) is visible. In figure (c) the circles with error bars (red in the web version of the article) describe the experimental kinetics data averaged from the black areas within the zone shown in the square. Triangles and the dash line in figure (c) represent the kinetics simulated using Eq. (4). (For interpretation of the references to colour in this figure legend, the reader is referred to the web version of this article).

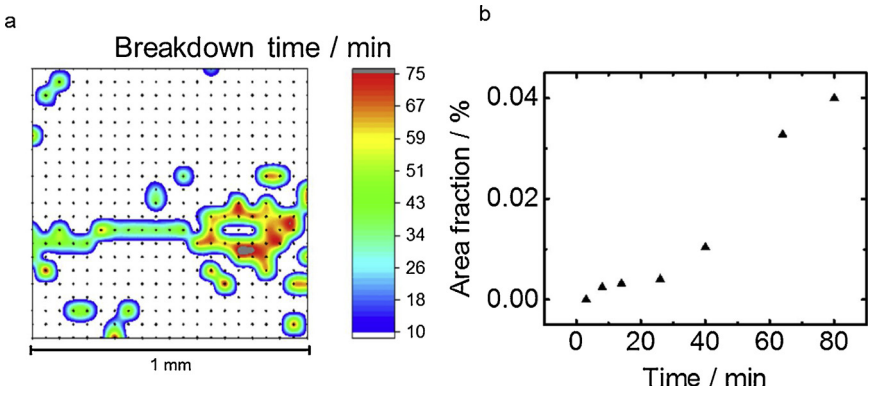

Fig. 7. Example of filiform corrosion advancement evaluated from the time of the sharp increase in kinetics curves obtained from Raman data (as illustrated in Fig. 6c). Spontaneous reaction of Mg 1 in 0.1 M NaCl solution at initial pH 9.5. Two representations based on the local kinetics of brucite growth are given. (a) Kinetic map in which the time when the kinetics curve shows a sharp increase of brucite quantity is shown by the color code for each point. This figure can be compared to the visual in optical microscope surface evolution in the same experiment (Fig. 2). (b) Fraction of the surface with "broken" film determined from Fig. 7a as a function of time.

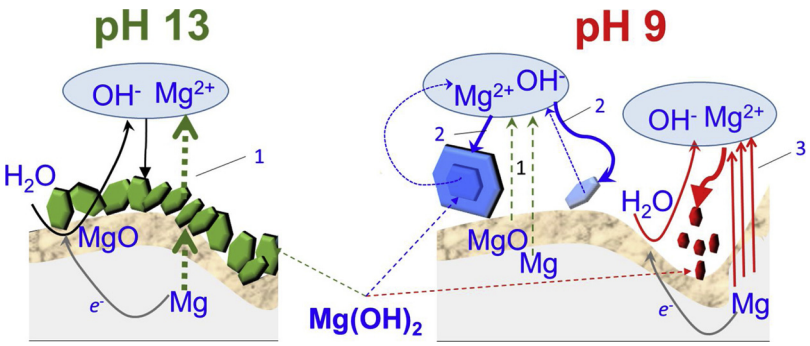

Fig. 8. Schematic representation of local dissolution – precipitation processes in initial stages of aqueous corrosion of Mg. Arrows show.
(1) Mg^{2+} diffusion through the oxide-hydroxide film;
(2) brucite grain growth for low energy surfaces (and dissolution of high energy surfaces); (3) processes leading to rapid nucleation because of local supersaturation after the oxide/hydroxide film thinning in the filament head and following pH increase at the neighboring cathodic areas.
Steps, expected from KRM to be responsible for the growth rate and crystal morphology in different conditions are: (1) at pH > 11, (2) at pH 7–10 in intact areas and (3) in case of the local film breakdown. (For interpretation of the references to colour in the text, the reader is referred to the web version of this article.)

formation of bigger crystals. Measured linear growth kinetics in these conditions is coherent with the surface reaction limited growth [82]. This surface limiting process on the existing nucleated crystals is logic because no diffusion of species is necessary due to high solubility of Mg $(OH)_2$ at this pH. The formation of bigger crystals with well-developed basal planes can be ascribed to continuous grain growth by dissolution precipitation process of a very limited number of nuclei with dissolution of the surfaces with high surface energy and development of low energy surfaces as schematically presented by arrows numbered "2" in Fig. 8 (center, colored in blue in the web version of the paper). The linear kinetics of the film growth is also coherent with the kinetics of the electrochemical precipitation of brucite from Mg^{2+} solutions under applied cathodic currents [96]. These continuous dissolution-precipitation processes and big crystal size should lead to higher porosity and easy incorporation of Cl^- in depth of the film. It should also facilitate the hydration of the inner MgO.

4.2. $Mg(OH)_2$ film evolution on corroded Mg explained by precipitation from supersaturated solution

The effect of pH on the evolution of the crystal size and morphology, on the film growth kinetics and on its resulting properties could be hence easily attributed to the dominance of one of the processes [97]: nucleation (pH 13) or the growth of the crystals from a solution (in case of pH 9) or [98]. Taking into account that anodic and cathodic reactions

$$Mg \rightarrow Mg^{2+} + 2e^- \quad (1)$$

$$H_2O + 2e^- \rightarrow H_2 + 2OH^- \quad (2)$$

inject ions near the surface, a supersaturation can be locally achieved resulting in the precipitation processes. It is well known, that even in flowing electrolyte there is an unmixed Nerst diffusion layer near the surface (with thickness defined differently in different references, but often considered as about 20–50 μm for moderate stirring and laminar flow [99,100]. The local concentration in this layer can be hence significantly higher than the bulk concentration [101,102], while even bulk concentration increased after the cell with time, which was also seen in our work from the bulk solution pH. In our experiments, solution did not flow continuously, it was systematically renewed using a syringe pump between mapping (every 5 or 10 min) in order to remove the bubbles. Moreover, the cell geometry (position of in and out channels) results in even bigger diffusion layer thickness. By consequence, a localized reactivity increase (by surface film breakdown or by a presence of a local cathode like noble impurity), can result in an excess of the local ions concentration at the solid / liquid interface compared to equilibrium concentration (supersaturation).

Considering solution supersaturation, Π, defined as the difference between the real measured concentrations and the solubility product at a given temperature (Eq. (3)):

$$\Pi = \frac{[Mg^{2+}][OH^-]^2}{[Mg^{2+}]_{eq}[OH^-]^2_{eq}} \quad (3)$$

it is easy to verify that for Mg^{2+} high supersaturations are easily achieved at high pH ([86]), favoring nucleation, whereas at pH < 11.5, for the same quantity of leached Mg^{2+} supersaturation level will be low and the crystal growth is favored vs nucleation.

Assuming the film growth in the approach of precipitation from supersaturated solutions [103] and taking into account that in corrosion the concentration of ions in the solution evolves with corrosion process, one can explain also the threshold-like kinetics of the brucite growth and formation of small crystals observed in black filaments. Indeed, at low supersaturation levels, small changes of concentration significantly modify the precipitation rate [104]. The reactivity at the black filaments is usually described as cathodic activation with anodic Mg^{2+} release at the filament head and the following cathodic H_2 evolution and pH increase [42,47,105]. This should lead to the local ionic supersaturation at the border between the dark and intact areas and result in enhanced precipitation as schematically presented by arrows numbered "3" (red in the web version of the figure) in Fig. 8.

Considering this process in the approach of the relaxation of supersaturated solutions [106,107], the precipitation rate should be

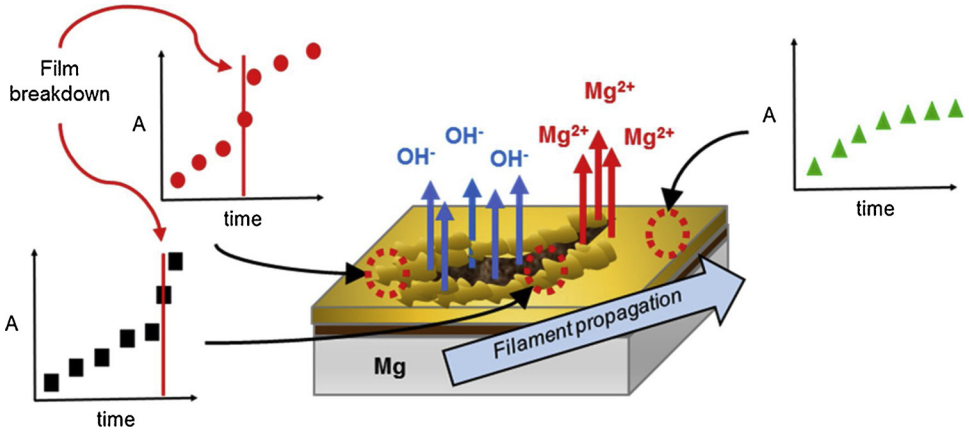

Fig. 9. Schematic representation of the effect of filiform corrosion on the local $Mg(OH)_2$ film growth kinetics.

proportional to the supersaturation factor Π and the surface area of the formed precipitates. Assuming hemispheric particles for which the surface is $\propto \sqrt[3]{m^2}$ and assuming that the area of the bulk Raman peak (A) reflects the quantity of the precipitated brucite, the brucite growth rate can be expressed as

$$A = \int_0^t k'' m_{Mg(OH)_2}^{\frac{2}{3}} \Pi(t) dt \quad (4)$$

where k" is a proportionality coefficient.

Using Eq. (4) and the experimental growth rates of the intact film at pH 9, the tree-step film growth kinetics distinguishable in Fig. 6c can be simulated (simulated curve is shown by a dash line). These three steps correspond to the following processes:

1) initial linear growth of the film thickness is ensured by a constant Mg^{2+} release from the substrate, which is not diffusion limited because of low barrier properties of a formed surface film;
2) at 90 min the surface film breakdown results in the activation of local anodic and cathodic reactions and the injection of the excess Mg^{2+} and OH^- ions. Assuming the local pH increase by 1 unit (from 9 to 10) and approximating the "supplementary" precipitation by Eq. (4) a sharp increase of the growth kinetics is easily obtained;
3) once the injected ions precipitate, the film re-passivates, the local interface pH value reaches a steady state and the reaction kinetics resembles kinetics in step 1.

The proposed schema of the evolution of the local brucite film growth kinetics with the propagation of filament corrosion is presented in Fig. 9.

5. Conclusions

To sum up, for the first time the effect of solution modification on the local evolution of the surface films at initial stages of Mg corrosion in thin layer cell was described by in-situ measurement. More precisely, the following conclusions can be drawn from the present work.

1) Novel in-situ kinetics Raman mapping (KRM) was developed which is able to map the local film growth and breakdown and extract kinetics laws on mm large surfaces with about 10 µm spatial and about 3 min time resolution within the same experiment. From the methodological point of view, the developed in-situ KRM could be easily extended to multiple processes for which in-situ measurement with local resolution can be of interest.
2) For the first time, the in-situ Raman spectra confirmed that crystalline brucite film forms and grows in situ on the surface of Mg during aqueous corrosion.
3) The local kinetics of brucite growth was correlated with the surface appearance and the local pH. For the areas, which did not evolve in optical images during immersion, brucite growth kinetics was parabolic (diffusion limited) at pH 13 but linear (surface reaction limited) at pH 7–10.5. A jump in the kinetics curve was observed in some particular locations. Statistical data treatment showed that this type of kinetics is associated with the proximity of black filaments and that the time of the steep increase in kinetics curve coincides with the first visual observation of filaments in studied zones.
4) The fine analysis of the high frequency Raman region was used to describe the evolution of the crystal size and morphology. The "satellite" peaks reflecting surface vibrations and the crystallographic orientation of the surface [89], the satellites which appeared only in conditions of high local pH evidenced the high surface area (small grain size) of in situ formed $Mg(OH)_2$ in these conditions, which was confirmed by ex-situ Scanning Electron Microscopy (SEM). A constant ratio between peaks reflecting different surfaces after 10 min induction period indicated a steady brucite particles shape at this pH.
5) The dissolution - precipitation mechanism of brucite film formation and breakdown was verified by its coherence with the observed kinetics of the brucite film growth, the crystals size and morphology at different pH. For this aim a model expecting nucleation and growth due to the ion release and increasing supersaturation caused by anodic and cathodic reactivity was proposed which can model an enhanced growth of $Mg(OH)_2$ in the proximity of filaments.

Appendix A. Supplementary data

Supplementary material related to this article can be found, in the online version, at doi:https://doi.org/10.1016/j.corsci.2019.03.024. The references [108–113] are used in this supplementary material.

References

[1] S.N. Mathaudhu, A.A. Luo, N.R. Neelameggham, E.A. Nyberg, W.H. Sillekens, Essential Readings in Magnesium Technology, Springer International Publishing, Cham, 2014, https://doi.org/10.1002/9781118859803.
[2] M. Esmaily, J.E. Svensson, S. Fajardo, N. Birbilis, G.S. Frankel, S. Virtanen, R. Arrabal, S. Thomas, L.G. Johansson, Fundamentals and advances in magnesium alloy corrosion, Prog. Mater. Sci. 89 (2017) 92–193, https://doi.org/10.1016/j.pmatsci.2017.04.011.
[3] A. Atrens, G.-L. Song, M. Liu, Z. Shi, F. Cao, M.S. Dargusch, Review of recent developments in the field of magnesium corrosion, Adv. Eng. Mater. 17 (2015) 400–453, https://doi.org/10.1002/adem.201400434.
[4] M. Taheri, R.C. Phillips, J.R. Kish, G.A. Botton, Analysis of the surface film formed on Mg by exposure to water using a FIB cross-section and STEM-EDS, Corros. Sci. 59 (2012) 222–228, https://doi.org/10.1016/j.corsci.2012.03.001.
[5] M.P. Brady, G. Rother, L.M. Anovitz, K.C. Littrell, K.A. Unocic, H.H. Elsentriecy, G.-L. Song, J.K. Thomson, N.C. Gallego, B. Davis, Film breakdown and nano-

porous Mg(OH)2 formation from corrosion of magnesium alloys in salt solutions, J. Electrochem. Soc. 162 (2015) C140–C149, https://doi.org/10.1149/2.0171504jes.
[6] M. Taheri, J.R. Kish, N. Birbilis, M. Danaie, E.A. McNally, J.R. McDermid, Towards a physical description for the origin of enhanced catalytic activity of corroding magnesium surfaces, Electrochim. Acta 116 (2014) 396–403, https://doi.org/10.1016/j.electacta.2013.11.086.
[7] J.H. Nordlien, S. Ono, N. Masuko, K. Nisancioglu, Morphology and structure of oxide films formed on magnesium by exposure to air and water, J. Electrochem. Soc. 142 (1995) 3320–3322, https://doi.org/10.1149/1.2049981.
[8] J.H. Nordlien, S. Ono, N. Masuko, K. Nisancioglu, A TEM investigation of naturally formed oxide films on pure magnesium, Corros. Sci. 39 (1997) 1397–1414, https://doi.org/10.1016/S0010-938X(97)00037-1.
[9] M. Liu, S. Zanna, H. Ardelean, I. Frateur, P. Schmutz, G. Song, A. Atrens, P. Marcus, A first quantitative XPS study of the surface films formed, by exposure to water, on Mg and on the Mg-Al intermetallics: Al3Mg2 and Mg17Al12, Corros. Sci. 51 (2009) 1115–1127, https://doi.org/10.1016/j.corsci.2009.02.017.
[10] M. Liu, P. Schmutz, S. Zanna, A. Seyeux, H. Ardelean, G. Song, A. Atrens, P. Marcus, Electrochemical reactivity, surface composition and corrosion mechanisms of the complex metallic alloy Al3Mg2, Corros. Sci. 52 (2010) 562–578, https://doi.org/10.1016/j.corsci.2009.10.015.
[11] C. Henrist, J. Mathieu, C. Vogels, A. Rulmont, R. Cloots, Morphological study of magnesium hydroxide nanoparticles precipitated in dilute aqueous solution, J. Cryst. Growth 249 (2003) 321–330.
[12] Y.M. Yan, O. Gharbi, A. Maltseva, X.B. Chen, Z.R. Zeng, S.W. Xu, W.Q. Xu, P. Volovich, Investigating the structure of the surface film on a corrosion resistant Mg-Li (-Al-Y-Zr) alloy, Corrosion 75 (2019) 80–89, https://doi.org/10.5006/2995.
[13] W. Vlug, O. Plümper, M. Kandianis, A. Blaaderen, Mvan H. Huis, In-situ hydration of MgO nanocrystals to amorphous Mg(OH)2 using liquid cell transmission electron microscopy, Eur. Microsc. Congr. 2016 Proc. Wiley-VCH Verlag GmbH & Co. KGaA., 2016, https://doi.org/10.1002/9783527808465.EMC2016.6823.
[14] P.-W. Chu, E. Marquis, Microstructural Aspects of Localized Corrosion Behavior of Mg Alloys, University of Michigan, 2017.
[15] G. Song, A. Atrens, D. Stjohn, J. Nairn, Y. Li, The electrochemical corrosion of pure magnesium in 1 N NaCl, Corros. Sci. 39 (1997) 855–875, https://doi.org/10.1016/S0010-938X(96)00172-2.
[16] N. Hara, Y. Kobayashi, D. Kagaya, N. Akao, Formation and breakdown of surface films on magnesium and its alloys in aqueous solutions, Corros. Sci. 49 (2007) 166–175, https://doi.org/10.1016/j.corsci.2006.05.033.
[17] G.L. Song, Corrosion Electrochemistry of Magnesium (Mg) and its Alloys, Woodhead Publishing Limited, 2011, https://doi.org/10.1533/9780857091413.1.3.
[18] A. Atrens, G.-L. Song, F. Cao, Z. Shi, P.K. Bowen, Advances in Mg corrosion and research suggestions, J. Magnes. Alloy 1 (2013) 177–200, https://doi.org/10.1016/j.jma.2013.09.003.
[19] S. Johnston, Z. Shi, A. Atrens, The influence of pH on the corrosion rate of high-purity Mg, AZ91 and ZE41 in bicarbonate buffered Hanks' solution, Corros. Sci. 101 (2015) 182–192, https://doi.org/10.1016/j.corsci.2015.09.018.
[20] S. Li, A.C. Bacco, N. Birbilis, H. Cong, Passivation and potential fluctuation of Mg alloy AZ31B in alkaline environments, Corros. Sci. 112 (2016) 596–610, https://doi.org/10.1016/j.corsci.2016.08.022.
[21] G.L. Makar, J. Kruger, Corrosion of magnesium, Int. Mater. Rev. 38 (1993).
[22] M.E. Straumanis, B.K. Bhatia, Disintegration of magnesium while dissolving anodically in neutral and acidic solutions, J. Electrochem. Soc. 110 (1963) 357–360, https://doi.org/10.1149/1.2425763.
[23] G.R. Hoey, M. Cohen, Corrosion of anodically and cathodically polarized magnesium in aqueous media, J. Electrochem. Soc. 105 (1958) 245, https://doi.org/10.1149/1.2428817.
[24] Z.P. Cano, M. Danaie, J.R. Kish, J.R. McDermid, G.A. Botton, G. Williams, Physical characterization of cathodically-activated corrosion filaments on magnesium alloy AZ31B, Corrosion 71 (2015) 146–159, https://doi.org/10.5006/1384.
[25] L. Wang, B.-P. Zhang, T. Shinohara, Corrosion behavior of AZ91 magnesium alloy in dilute NaCl solutions, Mater. Des. 31 (2010) 857–863, https://doi.org/10.1016/j.matdes.2009.07.049.
[26] T.W. Cain, I. Gonzalez-Afanador, N. Birbilis, J.R. Scully, The role of surface films and dissolution products on the negative difference effect for magnesium: comparison of Cl − versus Cl − free solutions, J. Electrochem. Soc. 164 (2017) C300–C311, https://doi.org/10.1149/2.1371706jes.
[27] S. Feliu Jr., M.C. Merino, R. Arrabal, A.E. Coy, E. Matykina, XPS study of the effect of aluminium on the atmospheric corrosion of the AZ31 magnesium alloy, Surf. Interface Anal. 41 (2009) 143–150, https://doi.org/10.1002/sia.3004.
[28] J.R. Kish, Y. Hu, J. Li, W. Zheng, J.R. McDermid, Technical note: examination of focused ion beam-sectioned surface films formed on am60b mg alloy in an aqueous saline solution, Corrosion 68 (2012) 468–474, https://doi.org/10.5006/i0010-9312-68-6-468.
[29] R. Sharma, M.J. McKelvy, H. Béarat, A.V.G. Chizmeshya, R.W. Carpenter, In-situ nanoscale observations of the Mg(OH)2 dehydroxylation and rehydroxylation mechanisms, Philos. Mag. 84 (2004) 2711–2729, https://doi.org/10.1080/14786430410001671458.
[30] K.A. Unocic, H.H. Elsentriecy, M.P. Brady, H.M. Meyer, G.L. Song, M. Fayek, R.A. Meisner, B. Davis, Transmission electron microscopy study of aqueous film formation and evolution on magnesium alloys, J. Electrochem. Soc. 161 (2014) C302–C311, https://doi.org/10.1149/2.024406jes.
[31] J.H. Lee, J.H. Eun, S.G. Kim, S.Y. Park, M.J. Lee, H.J. Kim, Hydration behavior of MgO single crystals and thin films, J. Mater. Res. 18 (2003) 2895–2903, https://doi.org/10.1557/JMR.2003.0404.
[32] D.A. Vermilyea, C.F. Kirk, Studies of inhibition of magnesium corrosion, J. Electrochem. Soc. 116 (1969) 1487–1492, https://doi.org/10.1149/1.2411579.
[33] G. Williams, H. Dafydd, R. Subramanian, Chloride ion concentration effects on passivity breakdown in magnesium, Electrochem. Soc. Trans. 58 (2014) 23–34, https://doi.org/10.1149/05831.0023ecst.
[34] S.H. Salleh, S. Thomas, J.A. Yuwono, K. Venkatesan, N. Birbilis, Enhanced hydrogen evolution on Mg(OH)2 covered Mg surfaces, Electrochim. Acta 161 (2015) 144–152, https://doi.org/10.1016/j.electacta.2015.02.079.
[35] Y. Yang, F. Scenini, M. Curioni, A study on magnesium corrosion by real-time imaging and electrochemical methods: relationship between local processes and hydrogen evolution, Electrochim. Acta 198 (2016) 174–184, https://doi.org/10.1016/j.electacta.2016.03.043.
[36] W. Sun, S. Nesic, Basics revisited: kinetics of iron carbonate scale precipitation in CO2 corrosion, NACE, NACE International, San Diego, California, 2006, pp. 1–26.
[37] A.D. Atrens, I. Gentle, A. Atrens, Possible dissolution pathways participating in the Mg corrosion reaction, Corros. Sci. 92 (2015) 173–181, https://doi.org/10.1016/j.corsci.2014.12.004.
[38] G. Song, A. Atrens, Understanding magnesium corrosion—a framework for improved alloy performance, Adv. Eng. Mater. 5 (2003) 837–858, https://doi.org/10.1002/adem.200310405.
[39] P. Dauphin-Ducharme, J. Mauzeroll, Surface analytical methods applied to magnesium corrosion, Anal. Chem. 87 (2015) 7499–7509, https://doi.org/10.1021/ac504576g.
[40] G. Williams, N. Birbilis, H.N. Mcmurray, The source of hydrogen evolved from a magnesium anode, Electrochem. commun. 36 (2013) 1–5, https://doi.org/10.1016/j.elecom.2013.08.023.
[41] S.V. Lamaka, J. Gonzalez, D. Mei, F. Feyerabend, R. Willumeit-Römer, M.L. Zheludkevich, Local pH and its evolution near Mg alloy surfaces exposed to simulated body fluids, Adv. Mater. Interfaces (2018) 1800169, https://doi.org/10.1002/admi.201800169 1–18001696.
[42] S.V. Lamaka, O.V. Karavai, A.C. Bastos, M.L. Zheludkevich, M.G.S. Ferreira, Monitoring local spatial distribution of Mg2+, pH and ionic currents, Electrochem. commun. 10 (2008) 259–262, https://doi.org/10.1016/j.elecom.2007.12.003.
[43] S. Lebouil, O. Gharbi, P. Volovitch, K. Ogle, Mg dissolution in phosphate and chloride electrolytes: insight into the mechanism of the negative difference effect, Corrosion 71 (2015) 234–241.
[44] J. Światowska, P. Volovitch, K. Ogle, The anodic dissolution of Mg in NaCl and Na2SO4 electrolytes by atomic emission spectroelectrochemistry, Corros. Sci. 52 (2010) 2372–2378, https://doi.org/10.1016/j.corsci.2010.02.038.
[45] O. Gharbi, N. Birbilis, Clarifying the dissolution mechanisms and electrochemistry of Mg2Si as a function of solution pH, J. Electrochem. Soc. 165 (2018) C497–C501, https://doi.org/10.1149/2.1061809jes.
[46] M. Curioni, F. Scenini, T. Monetta, F. Bellucci, Correlation between electrochemical impedance measurements and corrosion rate of magnesium investigated by real-time hydrogen measurement and optical imaging, Electrochim. Acta 166 (2015) 372–384, https://doi.org/10.1016/j.electacta.2015.03.050.
[47] G. Williams, H.N. Neil McMurray, Localized corrosion of magnesium in chloride-containing electrolyte studied by a scanning vibrating electrode technique, J. Electrochem. Soc. 155 (2008) C340–C349, https://doi.org/10.1149/1.2918900.
[48] G.S. Frankel, A. Samaniego, N. Birbilis, Evolution of hydrogen at dissolving magnesium surfaces, Corros. Sci. 70 (2013) 104–111, https://doi.org/10.1016/j.corsci.2013.01.017.
[49] K. Gusieva, C.H.J. Davies, J.R. Scully, N. Birbilis, Corrosion of magnesium alloys: the role of alloying, Int. Mater. Rev. 60 (2015) 169–194, https://doi.org/10.1179/1743280414Y.0000000046.
[50] D.S. Gandel, N. Birbilis, M.A. Easton, M.A. Gibson, The influence of Mn on the corrosion of Al-free Mg alloys, 18th Int. Corros. Cong. 8 (2011) 1–9.
[51] G. Baril, N. Pébère, Corrosion of pure magnesium in aerated and deaerated sodium sulphate solutions, Corros. Sci. 43 (2001) 471–484, https://doi.org/10.1016/S0010-938X(00)00095-0.
[52] G. Baril, G. Galicia, C. Deslouis, N. Pébère, B. Tribollet, V. Vivier, An impedance investigation of the mechanism of pure magnesium corrosion in sodium sulfate solutions, J. Electrochem. Soc. 154 (2007) C108, https://doi.org/10.1149/1.2401056.
[53] L. Wang, T. Shinohara, B.P. Zhang, Influence of chloride, sulfate and bicarbonate anions on the corrosion behavior of AZ31 magnesium alloy, J. Alloys Compd. 496 (2010) 500–507, https://doi.org/10.1016/j.jallcom.2010.02.088.
[54] G. Wu, Y. Fan, A. Atrens, C. Zhai, W. Ding, Electrochemical behavior of magnesium alloys AZ91D, AZCe2, and AZLa1 in chloride and sulfate solutions, J. Appl. Electrochem. 38 (2008) 251–257, https://doi.org/10.1007/s10800-007-9433-y.
[55] D. Mercier, J. Światowska, S. Zanna, A. Seyeux, P. Marcus, Role of segregated iron at grain boundaries on Mg corrosion, J. Electrochem. Soc. 165 (2018) C42–C49, https://doi.org/10.1149/2.0621802jes.
[56] L.G. Bland, K. Gusieva, J.R. Scully, Effect of crystallographic orientation on the corrosion of magnesium: comparison of film forming and bare crystal facets using electrochemical impedance and raman spectroscopy, Electrochim. Acta 227 (2017) 136–151, https://doi.org/10.1016/j.electacta.2016.12.107.
[57] D. Höche, C. Blawert, S.V. Lamaka, N. Scharnagl, C. Mendis, M.L. Zheludkevich, The effect of iron re-deposition on the corrosion of impurity-containing magnesium, Phys. Chem. Chem. Phys. 18 (2015) 1279–1291, https://doi.org/10.1039/c5cp05577f.
[58] G.L. Song, A. Atrens, Corrosion mechanisms of magnesium alloys, Adv. Eng. Mater. 1 (1999) 11–33.
[59] A. Zoubir, Raman Imaging Techniques and Applications, 1st ed., Springer, Verlag, Berlin, Heidelberg, 2012, https://doi.org/10.1007/978-3-642-28252-2.

[60] A. Tomandl, M. Wolpers, K. Ogle, The alkaline stability of phosphate coatings II: in situ Raman spectroscopy, Corros. Sci. 46 (2004) 997–1011, https://doi.org/10.1016/S0010-938X(03)00183-5.

[61] P. Colomban, Potential and drawbacks of Raman (micro)spectrometry for the understanding of iron and steel corrosion, new trends dev, Automot. Syst. Eng. (2011) 567–584, https://doi.org/10.5772/13436.

[62] M.C. Bernard, A. Hugot-Le Goff, D. Massinon, N. Phillips, Underpaint corrosion of zinc-coated steel sheet studied by in situ Raman spectroscopy, Corros. Sci. 35 (1993), https://doi.org/10.1016/0010-938X(93)90356-L.

[63] P. Delichere, A. Hugot Le Goff, S. Joiret, Study of thin corrosion films by in situ Raman spectroscopy combined with direct observation of nuclear reactions, Surf. Interface Anal. 12 (1988) 419–423.

[64] D. Abourazzouk, A.H. Goff, Corrosion of Ni-Cr dental alloys studied by in situ Raman spectroscopy: role of beryllium, Corros. Sci. 35 (1993) 809–815.

[65] N. Boucherit, A. Hugot-Le Goff, S. Joiret, Raman studies of corrosion films grown on iron and iron-molybdenum (Fe-6Mo) in pitting conditions, Corros. Sci. 32 (1991) 497–507.

[66] R.L. Farrow, A.S. Nagelberg, Raman spectroscopy of surface oxides at elevated temperatures, Appl. Phys. Lett. 36 (1980) 945–947, https://doi.org/10.1063/1.91659.

[67] A.H. Goff, C. Pallotta, In situ Raman spectroscopy for the study of iron relation to solution composition passivity in A, J. Electrochem. Soc. 132 (1985) 2805–2806.

[68] T. Ohtsuka, K. Kubo, N. Sato, Raman spectroscopy of thin corrosion films on iron at 100–150 C in air, Corrosion 42 (1986) 476–481, https://doi.org/10.5006/1.3583054.

[69] D. Thierry, D. Persson, C. Leygraf, In-situ Raman spectroscopy combined with X-ray photoelectron spectroscopy and nuclear microanalysis for studies of anodic corrosion film formation on Fe-Cr single crystals, J. Electrochem. Soc. 135 (1988) 305, https://doi.org/10.1149/1.2095605.

[70] J. Weissenrieder, C. Leygraf, In situ studies of filiform corrosion of iron, J. Electrochem. Soc. 151 (2004) B165, https://doi.org/10.1149/1.1645263.

[71] R. Baddour-Hadjean, J.P. Pereira-Ramos, Raman micro spectrometry applied to the study of electrode materials for lithium batteries, Chem. Rev. 110 (2010) 1278–1319, https://doi.org/10.1021/Cr800344k.

[72] M.J. Pelletier, Quantitative analysis using Raman spectrometry, Appl. Spectrosc. 57 (2003) 20A–42A, https://doi.org/10.1366/000370203321165133.

[73] M. Assirelli, W. Xu, W. Chew, Reactor kinetics studies via process Raman spectroscopy, multivariate chemometrics, and kinetics modeling, Org. Process Res. Dev. 15 (2011) 610–621, https://doi.org/10.1021/op100337v.

[74] E. Dropsit, D. Chapron, P. Bourson, S. Hoppe, A. Durand, On the exploitation of optical signal from Raman spectroscopy for in-situ conversion monitoring of emulsion polymerization, AIP Conf. Proc. 1914 (2017), https://doi.org/10.1063/1.5016752.

[75] D. De Waal, A.M. Heyns, K.J. Range, A Raman spectroscopic determination of the kinetics of decomposition of ammonium chromate (NH4)2CrO4, J. Solid State Chem. 80 (1989) 170–177, https://doi.org/10.1016/0022-4596(89)90076-5.

[76] L.J. Bonales, V. Muñoz-Iglesias, D. Santamaría-Pérez, M. Caceres, D. Fernandez-Remolar, O. Prieto-Ballesteros, Quantitative Raman spectroscopy as a tool to study the kinetics and formation mechanism of carbonates, Spectrochim. Acta – Part A Mol. Biomol. Spectrosc. 116 (2013) 26–30, https://doi.org/10.1016/j.saa.2013.06.121.

[77] D. Iqbal, A. Sarfraz, A. Erbe, Gradient in defect density of ZnO nanorods grown by cathodic delamination, a corrosion process, leads to end-specific luminescence, Nanoscale Horiz. 3 (2018) 58–65, https://doi.org/10.1039/c7nh00111h.

[78] R. Rodriguez, S. Vargas, M. Estevez, F. Quintanilla, A. Trejo-Lopez, A.R. Hernández-Martínez, Use of Raman spectroscopy to determine the kinetics of chemical transformation in yogurt production, Vib. Spectrosc. 68 (2013) 133–140, https://doi.org/10.1016/j.vibspec.2013.06.004.

[79] S.-S. Li, Q.-Y. Guan, G. Meng, X.-F. Chang, J.-W. Wei, P. Wang, B. Kang, J.-J. Xu, H.-Y. Chen, Revealing chemical processes and kinetics of drug action within single living cells via plasmonic Raman probes, Sci. Rep. 7 (2017) 2296, https://doi.org/10.1038/s41598-017-02510-9.

[80] G. Goudec, P. Colomban, Raman spectroscopy of nanomaterials: how spectra relate to disorder, particle size and mechanical properties, Prog. Cryst. Growth Charact. Mater. 53 (2007) 1–56, https://doi.org/10.1016/j.pcrysgrow.2007.01.001.

[81] I.M. Clegg, N.J. Everall, B. King, H. Melvin, C. Norton, On-line analysis using Raman spectroscopy for process control during the manufacture of titanium dioxide, Appl. Spectrosc. 55 (2001) 1138–1150.

[82] E. Ghali, Corrosion Resistance of Aluminum and Magnesium Alloys: Understanding, Performance and Testing, John Wiley, 2010.

[83] B. Downs, S. Robinson, H. Yang, P. Mooney, RRUFF Project, Dep. Geosci. Univ., Arizona, 2015http://rruff.info/.

[84] A. Suslu, K. Wu, H. Sahin, B. Chen, S. Yang, H. Cai, T. Aoki, S. Horzum, J. Kang, F.M. Peeters, S. Tongay, Unusual dimensionality effects and surface charge density in 2D Mg(OH)2, Sci. Rep. 6 (2016) 20525, https://doi.org/10.1038/srep20525.

[85] D. Tushcel, Why are the Raman spectra of crystalline and amorphous solids different? Spectroscopy 32 (2017) 26–33.

[86] O.S. Pokrovsky, J. Schott, Experimental study of brucite dissolution and precipitation in aqueous solutions: surface speciation and chemical affinity control, Geochim. Cosmochim. Acta 68 (2004) 31–45, https://doi.org/10.1016/S0016-7037(03)00238-2.

[87] G. Williams, N. Birbilis, H.N. McMurray, Controlling factors in localised corrosion morphologies observed for magnesium immersed in chloride containing electrolyte, Faraday Discuss. 180 (2015), https://doi.org/10.1039/C4FD00268G.

[88] S.R. Soniya, V.M. Nair, Synthesis and characterization of nanostructured Mg(OH)2 and MgO, Int. J. Sci. Res. 5 (2016) 197–203, https://doi.org/10.1179/174328409X415020.

[89] T.R. Zeitler, J.A. Greathouse, J.D. Gale, R.T. Cygan, Vibrational analysis of brucite surfaces and the development of an improved force field for molecular simulation of interfaces, J. Phys. Chem. C 118 (2014) 7946–7953, https://doi.org/10.1021/jp411092b.

[90] T.S. Duffy, C. Meade, Y. Fei, H. Mao, R.J. Hemley, High-pressure phase transition in brucite, Mg(OH)2, Am. Mineral. 80 (1995) 222–230.

[91] Z.A. Matysina, The relative surface energy of hexagonal close-packed crystals, Mater. Chem. Phys. 60 (1999) 70–78, https://doi.org/10.1016/S0254-0584(99)00050-4.

[92] G. Williams, H.A. Llwyd Dafydd, R. Subramanian, H.N. McMurray, The influence of chloride ion concentration on passivity breakdown in magnesium, Corrosion 73 (2017) 471–481.

[93] B. Dabir, R.W. Peters, J.D. Stevens, Precipitation kinetics of magnesium hydroxide in a scaling system, Ind. Eng. Chem. Fundam. 21 (1982) 298–305, https://doi.org/10.1021/i100007a018.

[94] A.T. Fromhold, Kinetics of oxide film growth on metal crystals – I. Formulation and numerical solutions, J. Phys. Chem. Solids 24 (1963) 1081–1092, https://doi.org/10.1016/0038-1098(63)90400-9.

[95] A.T. Fromhold, Fundamental theory of the growth of thick oxide films on metals, J. Phys. Soc. Jpn. 48 (1980) 2022–2030, https://doi.org/10.1143/JPSJ.48.2022.

[96] K. Zeppenfeld, Electrochemical removal of calcium and magnesium ions from aqueous solutions, Desalination 277 (2011) 99–105, https://doi.org/10.1016/j.desal.2011.04.005.

[97] C.S. Grove, R.V. Jelinek, H.M. Schoen, Crystallization from solution, Adv. Chem. Eng. 3 (1962) 1–60, https://doi.org/10.1016/S0065-2377(08)60057-5.

[98] J.A. Dirksen, T.A. Ring, Fundamentals of crystallization: kinetic effects on particle size distributions and morphology, Chem. Eng. Sci. 46 (1991) 2389–2427, https://doi.org/10.1016/0009-2509(91)80035-W.

[99] C.W. Tobias, M. Eisenberg, C.R. Wilke, Diffusiom and convection in electrolysis - a theoritical review, J. Electrochem. Soc. 99 (1952) 359–365.

[100] R. Walker, N.S. Holt, Determination of the nernst diffusion layer thickness in the hydroson agitation tank, Surf. Technol. (1984), https://doi.org/10.1016/0376-4583(84)90053-0.

[101] S. Lamaka, R.M. Souto, M.G.S. Ferreira, In-situ visualization of local corrosion by scanning Ion-selective Electrode Technique (SIET), Microsc. Sci. Technol. Appl. Educ. (2010) 2162–2173, https://doi.org/10.1159/000346370.Postmortem.

[102] P. Volovitch, M. Serdechnova, K. Ogle, Aqueous corrosion of Mg-Al binary alloys: roles of Al and Mg, Corrosion 68 (2012) 557–570, https://doi.org/10.5006/i0010-9312-68-6-557.

[103] A.E. Nielsen, Kinetics of Precipitation, Pergamon P, New York, 1964.

[104] O.S. Pokrovsky, J. Schott, Experimental study of brucite dissolution and precipitation in aqueous solutions: surface speciation and chemical affinity control, Geochim. Cosmochim. Acta 68 (2004) 31–45, https://doi.org/10.1016/S0016-7037(03)00238-2.

[105] G. Williams, H.A.L. Dafydd, R. Grace, The localised corrosion of Mg alloy AZ31 in chloride containing electrolyte studied by a scanning vibrating electrode technique, Electrochim. Acta 109 (2013) 489–501, https://doi.org/10.1016/j.electacta.2013.07.134.

[106] G. Lefèvre, V. Pichot, M. Fédoroff, Controlling particle morphology during growth of bayerite in aluminate solutions, Chem. Mater. 15 (2003) 2584–2592, https://doi.org/10.1021/cm0310059.

[107] H.A. Straten, P.L. Bruyn, Precipitation from supersaturated aluminate solutions, J. Colloid Interface Sci. 102 (1984) 260–277.

[108] N.J. Everall, Modeling and measuring the effect of refraction on the depth resolution of confocal Raman microscopy, Appl. Spectrosc. 54 (2000) 772–782.

[109] J.H. Parker, D.W. Feldman, M. Ashkin, Raman scattering by optical modes of metals, in: G.B. Wright (Ed.), Light Scatt. Spectra Solids Proc. Int. Conf. Held New York Univ. Springer, Berlin, Heidelberg, 1969, pp. 389–397, , https://doi.org/10.1007/978-3-642-87357-7_42 Berlin, Heidelberg.

[110] J.R. Ferraro, Low-Frequency Vibrations of Inorganic and Coordination Compounds, Springer US, 2012, https://books.google.fr/books?id=BbrSBwAAQBAJ.

[111] J. Kapitán, M. Dračínský, J. Kaminský, L. Benda, P. Bouř, Theoretical modeling of magnesium Ion imprints in the Raman scattering of water, J. Phys. Chem. B 114 (2010) 3574–3582, https://doi.org/10.1021/jp9110508.

[112] E.S. Gnanakumar, R.R. Gowda, S. Kunjir, T.G. Ajithkumar, P.R. Rajamohanan, D. Chakraborty, C.S. Gopinath, MgCl2·6CH3OH: a simple molecular adduct and its influence as a porous support for olefin polymerization, ACS Catal. 3 (2013) 303–311, https://doi.org/10.1021/cs300730j.

[113] R.J. Capwell, Raman spectra of crystalline and molten MgCl2, Chem. Phys. Lett. 12 (1972) 443–446.